RESEARCH BRIEF

Trastuzumab Deruxtecan Resistance via Loss of HER2 Expression and Binding

Wanyi Chen[1,2], Avantika Gupta[1], Nicholas Mai[3], Sharanya Nag[1], Joshua S. Lau[4], Sukrit Singh[5], John D. Chodera[2,5], Bo Liu[1], Elisa de Stanchina[6], Fresia Pareja[7], Atif Ali Hashmi[7], Miriam M. Lieberman[3], Shanu Modi[3,8], Jacqueline Bromberg[3,8], Pedram Razavi[3,8], Joshua Z. Drago[3,8], and Sarat Chandarlapaty[1,2,3,4]

Downloaded from aacrjournals.org/cancerdiscovery/article-pdf/16/2/235/3731667/cd-25-0647.pdf by guest on 26 October 2026

ABSTRACT

Trastuzumab Deruxtecan (T-DXd) is clinically beneficial in HER2-positive and HER2-low metastatic breast cancer. However, therapeutic resistance emerges over time in most patients, with poorly defined resistance mechanisms. Through a molecular characterization of paired patient specimens before and after T-DXd treatment, we found that 49% cases had major decreases in HER2 expression at progression, and among them, 52% exhibited complete HER2 loss. Using isogenic model systems, we demonstrated that decreases in HER2 expression corresponded to reductions in T-DXd internalization and major increases in drug IC_{50} value for tumor growth inhibition. We further identified and validated *ERBB2* mutations in the trastuzumab binding interface (V597M and P593R) that promoted T-DXd resistance. As a strategy to overcome impaired T-DXd binding and internalization, we tested low-dose combinations of T-DXd with TROP2-directed antibody–drug conjugates (ADC) and found that these could more uniformly deliver DXd payloads and thereby overcome resistance mediated by HER2 loss.

SIGNIFICANCE: The mechanisms underlying clinical T-DXd resistance have not been established. We now report on two mechanisms of resistance that converge on loss of target binding and propose combinations of distinct ADCs with shared payloads as a strategy to overcome resistance by enhancing intratumor delivery.

See related commentary by O'Meara and Tarantino, p.195

[1]Human Oncology and Pathogenesis Program, Memorial Sloan Kettering Cancer Center, New York, New York. [2]Weill Cornell Graduate School, Weill Cornell Medicine, New York, New York. [3]Department of Medicine, Memorial Sloan Kettering Cancer Center, New York, New York. [4]Gerstner Sloan Kettering Graduate School, Memorial Sloan Kettering Cancer Center, New York, New York. [5]Computational and Systems Biology Program, Memorial Sloan Kettering Cancer Center, New York, New York. [6]Antitumor Assessment Core Facility, Memorial Sloan Kettering Cancer Center, New York, New York. [7]Department of Pathology and Laboratory Medicine, Memorial Sloan Kettering Cancer Center, New York, New York. [8]Weill Cornell Medical College, Weill Cornell Medicine, New York, New York.

Corresponding Authors: Joshua Z. Drago, Memorial Sloan Kettering Cancer Center, 1275 York Avenue, Box 20, New York, NY 10065. E-mail: dragoj@mskcc.org; and Sarat Chandarlapaty, chandars@mskcc.org

Cancer Discov 2026;16:235–49

doi: 10.1158/2159-8290.CD-25-0647

This open access article is distributed under the Creative Commons Attribution-NonCommercial-NoDerivatives 4.0 International (CC BY-NC-ND 4.0) license.

©2025 The Authors; Published by the American Association for Cancer Research

INTRODUCTION

Antibody–drug conjugates (ADC) represent a groundbreaking class of therapeutic agents that are designed to combine the specificity of antibodies with the efficacy of chemotherapy. These complex molecules consist of a mAb targeting tumor-specific antigens, a cytotoxic payload to eliminate cancer cells, and a linker that connects them. This unique design was motivated by the hope of allowing ADCs to selectively deliver potent chemotherapeutic agents directly to cancer cells while minimizing off-target effects, thereby offering enhanced efficacy and safety compared with traditional cytotoxic therapies. However, the true mechanism of ADC action is likely more complex than this original conception suggests (1, 2).

Among the most transformative ADCs are those targeting HER2, an oncoprotein overexpressed in 15% to 20% of breast cancers (3). Anti-HER2 ADCs, such as trastuzumab emtansine (T-DM1) and trastuzumab deruxtecan (T-DXd), have revolutionized the treatment landscape for HER2-positive breast cancer, demonstrating significantly improved clinical outcomes compared with stand-alone antibody or chemotherapy-based approaches (4–6). T-DXd consists of an anti-HER2 mAb trastuzumab conjugated to a potent topoisomerase I inhibitor payload (DXd) through a tetrapeptide-based cleavable linker at a ratio of 1:8 (7, 8). Recently, T-DXd has shown significant clinical benefit in HER2 IHC 2+/FISH-negative or IHC 1+ breast cancers, with some responses even observed in cases historically classified as HER2 0 (9, 10). This breakthrough has led to a reevaluation of classic IHC-based HER2 classification in breast cancer, introducing new categories such as HER2-low and -ultralow and extending the drug's approval beyond breast cancers historically defined as HER2-positive (11). These developments have raised critical questions about the role of target expression in *de novo* and acquired resistance to T-DXd.

Loss or downregulation of the target antigen has been proposed as a mechanism of ADC resistance (10, 12, 13). Whereas several studies suggest that ADC target expression correlates with response and/or mAb uptake (14–20), few studies have systematically addressed the relationship between target engagement and ADC resistance. In this study, we assessed the abundance of HER2 and its binding with T-DXd, finding that (i) downregulation or loss of HER2 expression (21, 22) and (ii) mutations that interrupt T-DXd binding sites, both significantly impair T-DXd's anticancer efficacy by reducing drug internalization. We demonstrate that because these cells retain sensitivity to the DXd payload, target-mediated T-DXd resistance can be overcome by delivering DXd via an alternative target (TROP2) and that low-dose multi-target ADC combinations represent a promising therapeutic strategy.

RESULTS

ERBB2 Extracellular Domain Mutations Can Cause T-DXd Resistance

Whereas somatic mutations that activate HER2 kinase activity have been associated with enhanced internalization and response to T-DXd (23, 24), mutations that might prevent T-DXd binding have not been examined. We conducted a clinicogenomic analysis of Memorial Sloan Kettering Cancer Center's (MSKCC) cohort of patients with HER2-low and HER2-positive metastatic breast cancer (MBC) who were both treated with T-DXd and had next-generation sequencing (NGS) performed (n = 451) at our institution from 2018 to 2024 to identify novel mutations that might affect residues within the trastuzumab binding domains (557–561, 570–575, 593–603; ref. 25). We identified three potentially relevant and previously unreported *ERBB2* mutations in our cohort. Two mutations [V597M and p.Q213* (c637C>T)] were found in pre–T-DXd samples from patients with clinically HER2-positive disease that had rapid progression on T-DXd [defined as <3 months progression-free survival (PFS)], overall suggesting *de novo* resistance (Fig. 1A). The third mutation (P593R) was found in a patient who instead had an exceptionally prolonged duration of response to T-DXd (~32 months) and developed the P593R mutation on a postprogression biopsy, implying acquired resistance.

ERBB2 V597M

Patient #1 had an estrogen receptor (ER)-positive HER2-positive MBC (HER2 2+, FISH-positive; Fig. 1B; Supplementary Fig. S1A), and exhibited rapid progression of her liver metastases after only two cycles of T-DXd for first-line treatment of metastatic disease. Hybrid-capture panel-based NGS of her liver metastasis was performed on T-DXd biopsy samples both before and after treatment using MSK-IMPACT (24). Both samples revealed an *ERBB2* V597M mutation that had not been described in clinical databases such as OncoKB (25).

Based on its location within the trastuzumab binding domain, we hypothesized that this mutation might impair T-DXd binding and therefore, drug efficacy. We first used the established cocrystal structures to inform molecular dynamic simulations (23). Simulation of the V597M mutation revealed a change in $\Delta\Delta G$ of 0.75 ± 0.10 kcal/mol, implying a less favored interaction between trastuzumab and the mutant HER2 (Fig. 1C). To experimentally evaluate the impact of this mutation, we engineered MCF10A cells overexpressing either the wild-type (WT) or mutant *ERBB2* under a doxycycline-inducible promoter. MCF10A is a breast epithelial cell line that has negligible endogenous HER2 expression, thus enabling direct comparisons of the impact of the transgenes. Three widely characterized breast cancer cell lines with varying degrees of *ERBB2* amplifications and IHC scores were included as controls: MCF-7 (HER2-low), ZR-75-1 (HER2-medium), and SK-BR-3 (HER2-high).

Without doxycycline induction, both MCF10A WT and V597M cells exhibited low basal HER2 levels, corresponding to IHC HER2-low. Upon doxycycline induction, they exhibited equivalently elevated expression levels of HER2 protein (Fig. 1D). The overexpressed HER2 proteins were able to traffic to the cell membrane as revealed by flow cytometry analysis (Fig. 1E) with mean fluorescence intensity (MFI) values falling between those of ZR-75-1 and SK-BR-3, indicating HER2 levels in the HER2-medium to -high range. Droplet digital PCR (ddPCR) was performed to further validate the presence of V597M mutation (Supplementary Fig. S1B).

Downloaded from aacrjournals.org/cancerdiscovery/article-pdf/16/2/235/3731667/cd-25-0647.pdf by guest on 26 October 2026

To assess whether the mutation impacted internalization of T-DXd, we conjugated a pH-sensitive dye (pHrodo) to T-DXd, allowing us to monitor T-DXd–HER2 endocytosis (Supplementary Fig. S1C; ref. 22). Doxycycline-induced HER2 WT led to a 2.9-fold (geometric mean quantified from FACS histogram) increase of surface HER2 and rapid T-DXd internalization (200-fold increase at 15 hours, Fig. 1F). By contrast, the 3.9-fold increase of surface HER2 V597M increased T-DXd internalization by only 19-fold. To evaluate the impact of these changes in internalization upon tumor growth, we assessed cell viability in both models. Continuous exposure to 1 μg/mL (6.66 nmol/L) T-DXd for 7 days resulted in a 53.75% decrease ($P = 0.0004$) in cell viability and corresponding decrease in IC_{50} value for MCF10A cells overexpressing WT HER2 compared with control (without doxycycline), whereas there was no significant change in cell viability or IC_{50} value between HER2 V597M overexpressing cells and control (Fig. 1G and H).

ERBB2 p.Q213 (c637C>T)*

Patient #2, whose cancer responded poorly to T-DXd, was found to have a *ERBB2* Q213* mutation. This patient had ER+ HER2 0 breast cancer treated with standard first-line endocrine therapy plus cyclin-dependent kinase-4/6 inhibitor, until biopsy of a rapidly progressing liver metastasis revealed newly HER2 3+ disease, prompting a switch to paclitaxel–carboplatin–trastuzumab–pertuzumab which resulted in a complete response lasting 17 months. At the time of next progression, she was switched to T-DM1, which provided disease control for an additional 10 months until she had progression. NGS performed on biopsies at this time compared with biopsies done at the initial diagnosis of HER2-positive disease confirmed clonal relatedness of these cancers, with both samples exhibiting the same *TP53* and *PIK3CA* mutations. However, the post–T-DM1 biopsy revealed an acquired *ERBB2* Q213* mutation. Copy-number analysis showed a persistent focal eightfold copy-number amplification at the *ERBB2* locus. The premature stop codon truncated the protein 5′ to the trastuzumab binding domain, and protein expression of HER2 became reduced (IHC = 2+). At this point, the disease rapidly progressed through multiple successive regimens, including capecitabine/trastuzumab/tucatinib (PFS = 5 months) and alpelisib/fulvestrant/trastuzumab (PFS = 4 months), with T-DXd ultimately lasting for <2 months prior to disease progression and death. Interestingly, mutational signature analysis of the post–T-DM1 sample revealed that 81.7% of the mutations were associated with APOBEC3 activity, with the Q213* (GTC > TAG) mutation occurring at a canonical APOBEC3-context site (26). This case underscores the potential role of APOBEC3 mutagenesis, which is a prevalent mutational process driving breast cancer evolution (27), contributing to resistance acquisition.

To further validate our findings, we introduced the Q213* mutation to the previously described MCF10A HER2 overexpression (OE) system. However, the truncated HER2 protein was not detectable by Western blot (Supplementary Fig. S1D). qPCR analysis confirmed that *ERBB2* mRNA levels were significantly ($P < 0.0001$) increased under 0.05 and 2 μg/mL doxycycline compared with the no-doxycycline control (Supplementary Fig. S1E). Despite this elevated transcription, the truncated HER2 failed to internalize T-DXd (Supplementary Fig. S1F) and did not enhance response to T-DXd treatment (Fig. 1I; Supplementary Fig. S1G).

ERBB2 P593R

In contrast to the two patients above, patient #3 was found to have a new *ERBB2* P593R mutation on postprogression biopsies after prolonged duration of response to T-DXd instead of before treatment. This patient was originally diagnosed with a *de novo* metastatic ER+ HER2 0 breast cancer that had rapid progression of disease on first-line fulvestrant + abemaciclib combination treatment. Somatic tumor NGS on liver metastasis at this time was notable for a well-characterized activating mutation in the *ERBB2* kinase domain (L755S) alongside a separate pathogenic *ERBB3* E928G mutation. Due to the *ERBB2* L755S mutation, she next received a combination of fulvestrant, neratinib, and trastuzumab on a clinical trial with good disease control for almost 2 years. The patient ultimately developed disease progression in the liver, with biopsy at that time continuing to demonstrate HER2 0 disease. However, given her known *ERBB2* activating mutation and good response to anti-HER2 therapies, she was transitioned to T-DXd, which provided excellent disease control for ~32 months. She was ultimately again found to have progression of disease in her liver. Somatic NGS of her liver tumor at this point redemonstrated the previously known *ERBB2* L755S and *ERBB3* E928G mutations, but it now also demonstrated a new *ERBB2* P593R mutation with a variant allele frequency comparable with the previously known *ERBB2* L755S (Fig. 1B). In this case, the change from a hydrophobic proline to a hydrophilic arginine occurs at the start of the AA 593 to 603 trastuzumab binding domain, resulting in increased volume and net positive charge (Supplementary Fig. S1H). The data thus imply that this is an acquired, clonal mutation associated with T-DXd progression. Overall, though these represent uncommon occurrences, the findings underscore how mutations affecting trastuzumab binding to HER2 can significantly diminish the efficacy of T-DXd treatment.

Likewise, we also established a HER2 P593R OE system and assessed total and surface HER2 levels by Western blot (Supplementary Fig. S1I) and FACS analysis (Supplementary Fig. S1J), respectively, under varying doxycycline concentrations, in comparison with the WT model. We found that inducing P593R expression with 0.01 μg/mL doxycycline resulted in HER2 levels comparable with those in the WT model induced with 0.2 μg/mL doxycycline in total protein and surface levels. Therefore, these conditions were used for subsequent functional studies.

Despite having higher HER2 expression levels, the P593R mutant showed reduced internalization of T-DXd (Supplementary Fig. S1K) and compromised responses to T-DXd treatment (Fig. 1J; Supplementary Fig. S1L).

Loss of HER2 Levels Leads to T-DXd Resistance

To investigate whether total HER2 expression might be reduced or lost at progression on T-DXd independent of *ERBB2* mutation status, we performed a retrospective analysis on a cohort of 102 patients with breast cancer treated with T-DXd.

Downloaded from aacrjournals.org/cancerdiscovery/article-pdf/16/2/235/3731667/cd-25-0647.pdf by guest on 26 October 2026

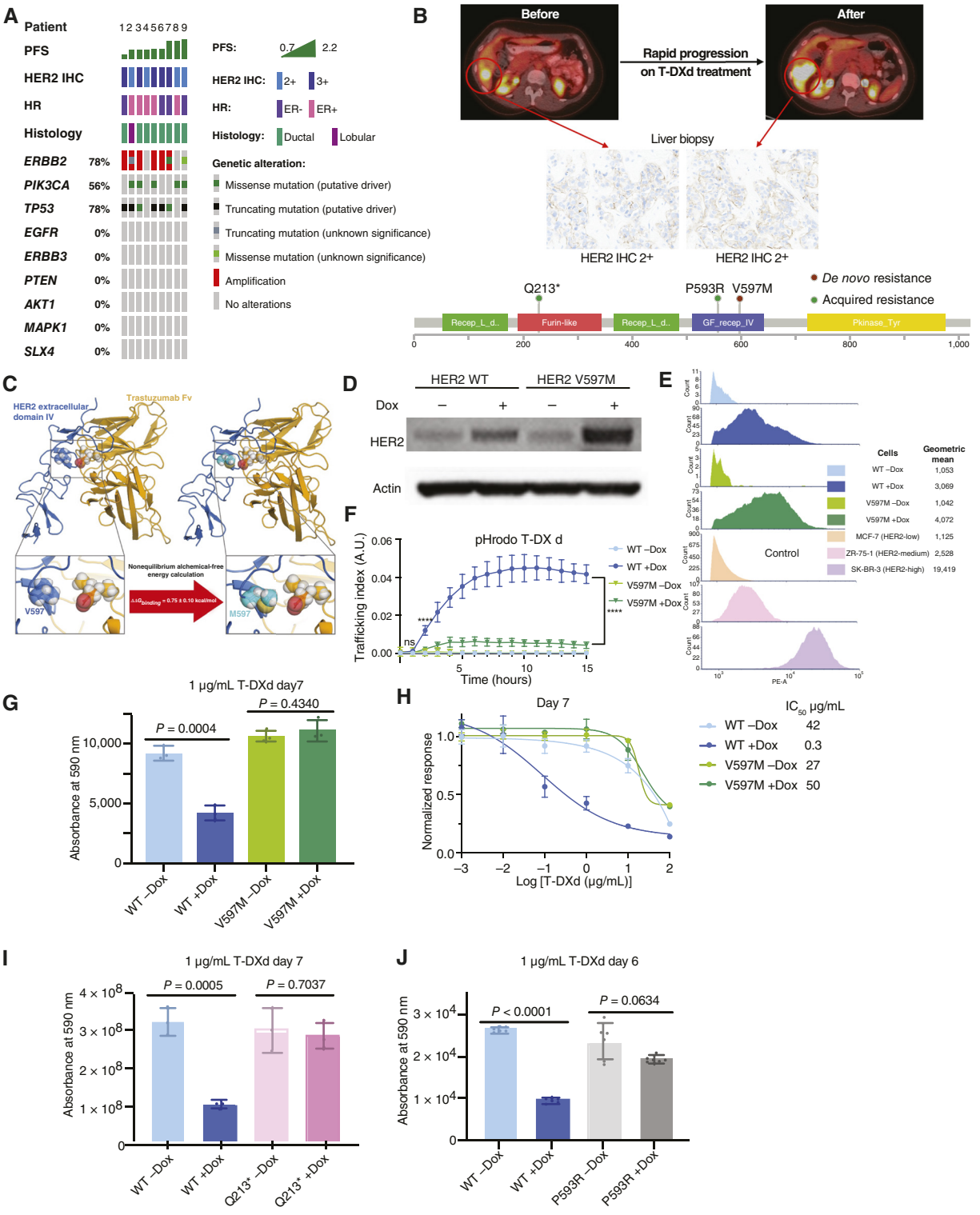


Figure 1. *ERBB2* ECD mutations and T-DXd resistance. **A,** Clinicogenomic data for nine patients with HER2+ MBC who had rapid progression to T-DXd (<3 months PFS) are shown in the oncoprint here, with each column representing a different patient. Two patients were found to have *ERBB2* mutations of interest: Patient #2 had Q213* mutation, and patient #9 had V597M variant of unknown significance (VUS). There were no noted mutations in *EGFR*, *ERBB3*, *PTEN*, *AKT1*, *MAPK1*, or *SLX4*. **B,** Top, radiographic and pathologic data from the patient with *ERBB2* V597M mutation who had rapid progression on T-DXd are shown. HER2 interval PET CTs showed rapid progression of known liver lesions between start of T-DXd and after 2 months of treatment. Middle, HER2 IHC staining showed no change to HER2 expression. Bottom, lollipop plot showed P593R and V597M mutation located within one of the trastuzumab binding regions, Q213* mutation resides within the *furin-like* cysteine-rich *region*. **C,** Alchemical-free energy calculations predict a decrease in binding affinity (red arrow) between extracellular domain IV of HER2 and the variable domain of the V597M trastuzumab mutant. (*continued on following page*)

Downloaded from aacrjournals.org/cancerdiscovery/article-pdf/16/2/235/3731667/cd-25-0647.pdf by guest on 26 October 2026

These patients had paired pretreatment and posttreatment samples and detectible HER2 expression by IHC on their most proximal pretreatment samples (28). Among these cases, we observed decreases of HER2 levels as measured by IHC in 50 cases (49%) and, among those, loss of HER2 expression down to IHC 0 was observed in 26 cases (52%; Fig. 2A). This finding has also been reported previously in smaller cohorts (10, 19). As IHC results can be affected by preanalytic variables such as tissue fixation and processing (29, 30), we sought to further validate the observed decrease in HER2 expression using an independent method. We performed immunofluorescence (IF) analysis on 15 pretreatment and 16 posttreatment patient samples, among which 9 were paired samples. A representative image is shown in Fig. 2B. Quantitative analysis demonstrated a significant reduction in HER2 staining intensity following T-DXd treatment ($P < 0.01$; Fig. 2B′), supporting the finding of HER2 expression loss observed by IHC. As a comparison, we identified 20 patients with MBC treated with the TROP2-targeted ADC sacituzumab govitecan (SG), who had detectable HER2 expression at baseline (1–2+) and had paired posttreatment biopsies available without intervening T-DXd therapy. Of these cases, only 1 (5%) was observed to have loss of HER2 expression (IHC 0) after treatment with SG. This supports the hypothesis that HER2 loss occurs more frequently under the selective pressure of a HER2-targeted ADC, rather than as a result of general tumor evolution or TOP1 inhibition.

Given the activity of T-DXd even in HER2-low breast cancer, we sought to determine whether loss of HER2 expression might be sufficient to promote T-DXd resistance. To address this, we generated isogenic models in which we could effectively lower the steady-state levels of HER2 expression, as was observed in these patients, across cellular contexts. Using an MCF10A model expressing a doxycycline-inducible *ERBB2* cDNA transgene as the only source of HER2 protein (Fig. 2C and D), we found that reducing the concentrations of doxycycline administered could lower HER2 expression to levels corresponding to clinical HER2 IHC scores such as 1+ and 0 (Fig. 2E). For generalizability, we constructed additional models with this method, including CAMA-1 [ER+/ progesterone receptor (PR)+/HER2 0 luminal type breast cancer cell line], 18cS1 [ER+/PR−/HER2 1+ primary cells derived from patient-derived xenograft (PDX)], T47D (ER+/PR+/HER2 2+ luminal type breast cancer cell line), and 293T (ER+/PR+/HER2+ human embryonic kidney cell; Supplementary Fig. S2A and S2B).

Utilizing pHrodo-labeled T-DXd, we found a strong correlation between HER2 expression levels and T-DXd internalization, with a nearly 50% decrease in internalization as doxycycline concentration decreased from 1 to 0.05 μg/mL ($P < 0.0001$) or from 0.05 to 0.01 μg/mL ($P < 0.0001$; Fig. 2F). In the absence of HER2 expression (0 μg/mL doxycycline), T-DXd internalization was negligible. By contrast, pHrodo-labeled human IgG conjugated with DXd showed no internalization even at the highest doxycycline concentration (1 μg/mL). Similar patterns were corroborated in the four additional models (Supplementary Fig. S2C), confirming that T-DXd internalization depends on HER2 expression.

To further validate the correlation between T-DXd internalization and HER2 expression levels, we performed ELISA assays to quantify intracellular and extracellular trastuzumab levels (Fig. 2G; Supplementary Fig. S2D and E). We found that intracellular trastuzumab levels significantly decreased ($P = 0.0389$) when doxycycline was reduced from 1 to 0.2 μg/mL. The decrease was more pronounced ($P = 0.0017$) between doxycycline 1 and 0.05 μg/mL and even greater ($P = 0.0002$ or $P = 0.0001$) when doxycycline was further reduced to 0.01 or 0 μg/mL. For extracellular trastuzumab levels, no significant difference was observed between doxycycline 0.2 and 0.05 μg/mL compared with 1 μg/mL (Supplementary Fig. S2E). However, significant increases ($P = 0.0105$ or $P = 0.0366$) were detected when doxycycline concentrations were further decreased to 0.01 or 0 μg/mL. These findings confirmed that lower HER2 expression levels led to decreased T-DXd internalization, which correlated with an increase in extracellular trastuzumab. Finally, to validate these findings using a non–pH-dependent approach to evaluate internalization, we labeled T-DXd with Alexa Fluor 488 and tracked its uptake in live cells upon drug exposure (Fig. 2H and H′). We observed a 99.43% ($P < 0.0001$) decrease of intracellular

Figure 1. ***(Continued)*** Top, representations of the variable region of trastuzumab (orange) in complex with the WT V597 (left) and mutant M597 (right) extracellular domain IV of HER2. Bottom, zoomed-in views of the WT V597 and mutated M597 residues, in which side-chain atoms are represented as dark blue and cyan spheres, respectively. Shown in the red arrow is the predicted relative binding free energy ($\Delta\Delta G_{binding}$) of trastuzumab binding HER2 following the V597M mutation. **D,** Western blot showing HER2 protein levels in MCF10A cells overexpressing HER2 WT and HER2 V597M after 48 hours of incubation with 0.2 μg/mL doxycycline (abbreviated as Dox in figures) or vehicle control. Representative plots are shown, with experiments performed independently three times. **E,** Flow cytometry analysis showing surface HER2 levels in MCF10A cells overexpressing HER2 WT and HER2 V597M after 48 hours of incubation with 0.2 μg/mL doxycycline or vehicle control. Geometric mean calculated by FCS Express was shown in the table. MCF7 (HER2-low), ZR-75-1 (HER2-medium), and SK-BR-3 (HER2-high) were included as standard controls. Experiments were repeated twice. **F,** Internalization of 5 μg/mL pHrodo Red–labeled T-DXd in MCF10A cells overexpressing HER2 WT and V597M with incubation of 0.2 μg/mL doxycycline or vehicle control. Data are presented as the mean ± SD of trafficking index from 12 images per time point. Representative plots from three independent experiments are shown. Statistical significance was determined using two-way ANOVA test with multiple comparisons. ****, $P < 0.0001$; ns, not significant ($P > 0.05$). **G,** Cell viability was assessed on day 7 for MCF10A cells overexpressing HER2 WT and V597M treated with 1 μg/mL T-DXd, with incubation of 0.2 μg/mL doxycycline or vehicle control. Data are presented as the mean ± SD, $n = 3$. Statistical significance was determined using an unpaired two-tailed *t* test. Experiments were repeated twice. **H,** Percentage of viable cells in MCF10A HER2 WT and V597M overexpressing cells treated with different concentrations of T-DXd with incubation of 0.2 μg/mL doxycycline or vehicle control. IC_{50} values were calculated using Prism software based on cell growth curves on day 7. Data are shown as the mean ± SD, $n = 3$. Experiments were repeated twice. **I,** Cell viability was assessed on day 7 for MCF10A cells overexpressing HER2 WT and Q213* treated with 1 μg/mL T-DXd, with incubation of 0.2 μg/mL doxycycline or vehicle control. Data are presented as the mean ± SD, $n = 3$. Statistical significance was determined using an unpaired two-tailed *t* test. Experiments were repeated twice. **J,** Cell viability was assessed on day 6 for MCF10A cells overexpressing HER2 WT (with incubation of 0.2 μg/mL doxycycline or vehicle control) and P593R (with incubation of 0.01 μg/mL doxycycline or vehicle control), treated with 1 μg/mL T-DXd. Data are presented as the mean ± SD, $n = 6$. Statistical significance was determined using an unpaired two-tailed *t* test. Experiments were repeated twice.

Downloaded from aacrjournals.org/cancerdiscovery/article-pdf/16/2/235/3731667/cd-25-0647.pdf by guest on 26 October 2026

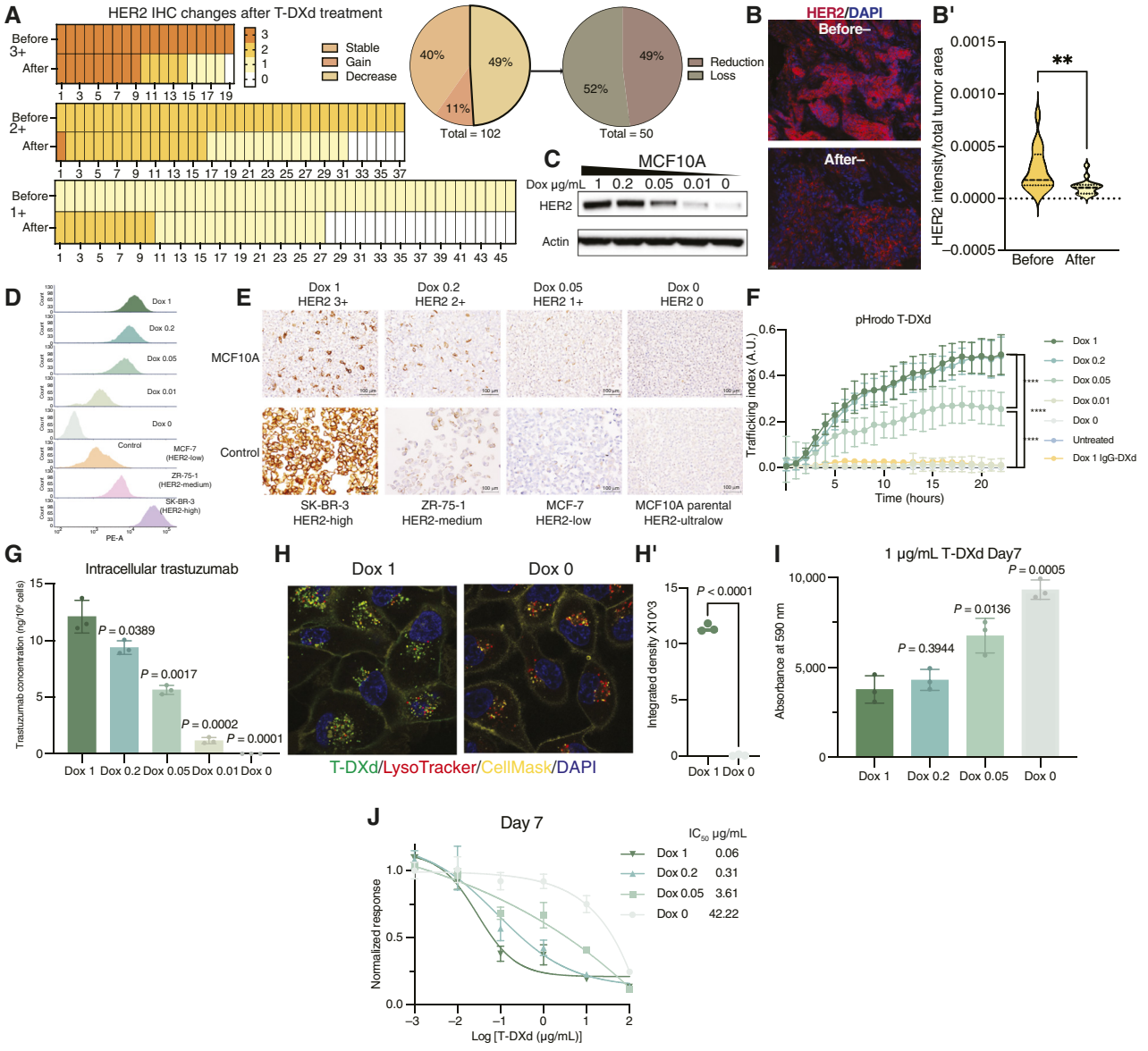


Figure 2. Loss of HER2 expression and T-DXd resistance. **A,** From a retrospective study performed on 102 patients with breast cancer with varying levels of baseline HER2 expression and treated with standard-of-care T-DXd, most patients had some degrees of HER2 downregulation when comparing real-world pretreatment and postprogression biopsies, both on HER2 IHC and NGS (24). **B,** Representative images of HER2 IF performed on paired pretreatment and posttreatment patient biopsy samples. **B′,** Quantification of temporal changes in HER2 staining measured by IF in 15 pretreatment and 16 posttreatment samples, including nine paired samples. *P* value was determined by an unpaired two tailed *t* test. **, $P < 0.01$. **C,** Western blot analysis of total HER2 expression levels in MCF10A cells induced by different concentrations of doxycycline for 48 hours. Representative blot is shown. The experiment was repeated independently three times. **D,** Flow cytometry analysis showing surface HER2 levels in MCF10A cells induced by different concentrations of doxycycline for 48 hours. MCF-7 (HER2-low), ZR-75-1 (HER2-medium), and SK-BR-3 (HER2-high) served as internal controls. Representative plot is shown, with the experiment repeated independently three times. **E,** IHC showing membrane HER2 levels in MCF10A cells induced by different concentrations of doxycycline for 48 hours, with IHC scores classified by pathologist. MCF10A parental (HER2 ultra-low), MCF-7 (HER2 low), ZR-75-1 (HER2 medium) and SK-BR-3 (HER2 high) were used as internal controls. **F,** Internalization of 5 µg/mL pHrodo Red labeled T-DXd in MCF10A cells treated with different concentrations of doxycycline. Human IgG conjugated with DXd was used as positive control. Data are presented as mean ± SD of trafficking index, $n = 12$. Representative plots were shown, with experiments repeated independently three times. Two-way ANOVA analysis with multiple comparisons was performed for each time point. *P* values for the final time point (22 hours) between Dox 1 and Dox 0.05, Dox 0.05 and Dox 0, and Dox 1 and Dox 0 are indicated (Dox 1 = 1 µg/mL, Dox 0.2 = 0.2 µg/mL, Dox 0.05 = 0.05 µg/mL, Dox 0.01 = 0.01 µg/mL, and Dox 0 = no Dox). ****, $P < 0.0001$. **G,** Quantification of intracellular trastuzumab concentrations by ELISA in MCF10A cells treated with 1 µg/mL T-DXd for 24 hours. Data are shown as the mean ± SD, $n = 3$. *P* values were determined by unpaired two tailed *t* test compared with Dox 1 condition. **H,** Confocal imaging showing intracellular Alexa Fluor 488–labeled T-DXd in MCF10A cells in Dox 1 and Dox 0 conditions. LysoTracker was used to mark localization of lysosomes. Statistical analysis is shown in **H′**. Integrated density of Alexa Fluor 488–labeled T-DXd was quantified by Fiji, $n = 3$. *P* values were determined by unpaired two-tailed *t* test. ****, $P < 0.0001$. **I,** Cell viability of MCF10A cells treated with 1 µg/mL T-DXd recorded on day 7 under different concentrations of doxycycline. Data are shown as the mean ± SD, $n = 3$. *P* values were determined by unpaired two-tailed *t* test compared with Dox 1 condition. Representative plots were shown, with experiments repeated independently three times. **J,** IC_{50} curves and values derived from cell growth curve data on day 7. Data are presented as the mean ± SD, $n = 3$. Representative plots were shown, with experiments repeated independently three times. DAPI, 4′,6-diamidino-2-phenylindole.

Downloaded from aacrjournals.org/cancerdiscovery/article-pdf/16/2/235/3731667/cd-25-0647.pdf by guest on 26 October 2026

T-DXd signal when doxycycline was reduced from 1 to 0 μg/mL, further supporting the relationship between expression level and drug internalization.

We next assessed the impact of reduced expression in the models upon cell viability across different T-DXd dosages and doxycycline concentrations (Fig. 2I; Supplementary Fig. S2F). The number of viable cells under treatment with 1 μg/mL T-DXd increased significantly ($P = 0.0136$) when doxycycline was reduced from 1 to 0.05 μg/mL, with a more pronounced increase ($P = 0.0005$) when it was further reduced to 0 μg/mL (Fig. 2I). The IC_{50} values increased fivefold when doxycycline concentration decreased from 1 to 0.2 μg/mL, 60-fold when reduced to 0.05 μg/mL, and 700-fold when further reduced to no doxycycline condition, reflecting the HER2 0 parental MCF10A cells (Fig. 2J). A similar pattern in change in viability was observed in other models tested (Supplementary Fig. S2G–S2I).

Taken together, the findings suggest that the reductions in HER2 expression observed in a subset of patients at T-DXd progression could sufficiently reduce T-DXd internalization to the point of clinical treatment resistance.

Combination Therapy of DXd-Based ADCs Targeting HER2 and TROP2 Synergizes to Overcome T-DXd Resistance

Given the reduction in T-DXd internalization caused by HER2 loss or mutation, we hypothesized that alternative strategies for enhancing DXd internalization might prove efficacious in this setting. Cells with low levels of HER2 remain sensitive to the naked DXd payload: with the addition of 0.01 μmol/L DXd to 1 μg/mL T-DXd, the cell growth inhibitory effect was significantly ($P < 0.0001$) improved compared with cells with high levels of HER2 treated with 1 μg/mL T-DXd only (Fig. 3A). As such, based upon these preliminary results, we hypothesized that adding a HER2-independent means to deliver DXd may maximize cytotoxic payload delivery and thus, anticancer potential.

The TROP2-directed ADC, datopotamab deruxtecan (Dato-DXd) delivers the same DXd payload as T-DXd albeit with a lower drug-to-antibody ratio of 4 and has shown single-agent efficacy in MBC (31–33). We utilized our panel of inducible HER2 models and found TROP2 is highly expressed across breast cancer cell lines as well as in MCF10A cells (Supplementary Fig. S3A). Such expression can also be detected by IHC staining (Supplementary Fig. S3B). We compared the efficacy of Dato-DXd across MCF10A cells at high versus low levels of HER2 and found that HER2 expression had no impact ($P > 0.05$) on Dato-DXd efficacy (Fig. 3B). These data also suggest that an alternative DXd delivery mechanism might still be useful when HER2 is lost. Given that TROP2 could hypothetically be lost as a mechanism of resistance to Dato-DXd, we tested combinations of T-DXd with Dato-DXd across a range of drug concentrations to forestall target-mediated resistance. Strikingly, we found that lower doses of T-DXd (1 μg/mL) and Dato-DXd (1 μg/mL) were as effective as higher dose of either single agent alone (10 μg/mL; Fig. 3C). Similar findings were observed in multiple models, including the MCF-7 HER2 OE cell line model, 18cS1 HER2 OE primary cell line model, as well as ZR-75-1 (HER2-medium breast cancer cell line; Supplementary Fig. S3C).

Labeling both T-DXd and Dato-DXd with pHrodo, we quantified the total trafficking index as an indirect measure of intracellular DXd levels (Fig. 3D). Cotreatment with 1 μg/mL T-DXd and 1 μg/mL Dato-DXd resulted in significantly higher intracellular DXd compared with treatment with either 10 μg/mL T-DXd ($P < 0.01$) or 10 μg/mL Dato-DXd ($P < 0.0001$) alone (Fig. 3D′). There was no significant difference in intracellular DXd levels across 1, 5, or 10 μg/mL T-DXd treatments ($P > 0.05$), nor between 1 and 5 μg/mL Dato-DXd treatments ($P > 0.05$; Supplementary Fig. S3D).

To evaluate the *in vivo* efficacy of the combination therapy, we randomized mice bearing 18cS1 xenografts and treated them with either T-DXd or Dato-DXd alone or the combination (Supplementary Fig. S3E). Whereas monotherapy with either ADC led to only modest tumor growth delay, the combination treatment significantly suppressed tumor growth, despite both ADCs sharing the same DXd payload.

To assess potential toxicity, we monitored body weight. Mice receiving a lower dose combination of T-DXd (3 mg/kg) and Dato-DXd (3 mg/kg) experienced less body weight loss than those treated with a high dose of T-DXd (10 mg/kg) alone (Supplementary Fig. S3E′), indicating improved tolerability.

Given concerns that combining ADCs with the same payload could exacerbate toxicity and reduce patient tolerability, we next tested whether a lower-dose combination could achieve similar efficacy. In a HER2-medium cell line–derived xenograft (CDX) model ZR-75-1 cells, mice treated with 1.5 mg/kg T-DXd + 1.5 mg/kg Dato-DXd exhibited greater tumor growth suppression compared with those treated with either 3 mg/kg T-DXd or 3 mg/kg Dato-DXd alone, with only the combination arm resulting in tumor regression (Fig. 3E). Moreover, no significant differences ($P > 0.05$) in body weight were observed among the groups, suggesting that the combination was well tolerated.

To investigate whether the enhanced therapeutic effect of the combination therapy was due to increased tumor payload delivery, we measured DXd concentrations in tumors and plasma 24 hours after treatment using LC-MS/MS (10, 34–36). The tumor-to-plasma DXd ratio in the combination group was significantly higher than that observed in the 3 mg/kg T-DXd group ($P < 0.05$) and comparable with that in the 3 mg/kg Dato-DXd group ($P > 0.05$; Fig. 3F).

These findings support the potential of ADC combinations to enhance intratumoral payload delivery and potentially evade target loss–mediated resistance.

DISCUSSION

The remarkable activity of T-DXd across both *ERBB2*-amplified and *ERBB2*-nonamplified breast cancer has revealed the multifaceted antitumor potential for ADCs. On one hand, the exceptional activity in HER2-overexpressing cancers gives proof of concept to the idea of using tumor-specific antigens to drive selective uptake of chemotherapy. On the other hand, the less dramatic activity observed in *ERBB2*-nonamplified breast cancer has revealed the potential for more promiscuous uptake, which may underlie ADC antitumor activity in the absence of clonal high-level target expression. Whereas several studies highlight the correlation between target

Downloaded from aacrjournals.org/cancerdiscovery/article-pdf/16/2/235/3731667/cd-25-0647.pdf by guest on 26 October 2026

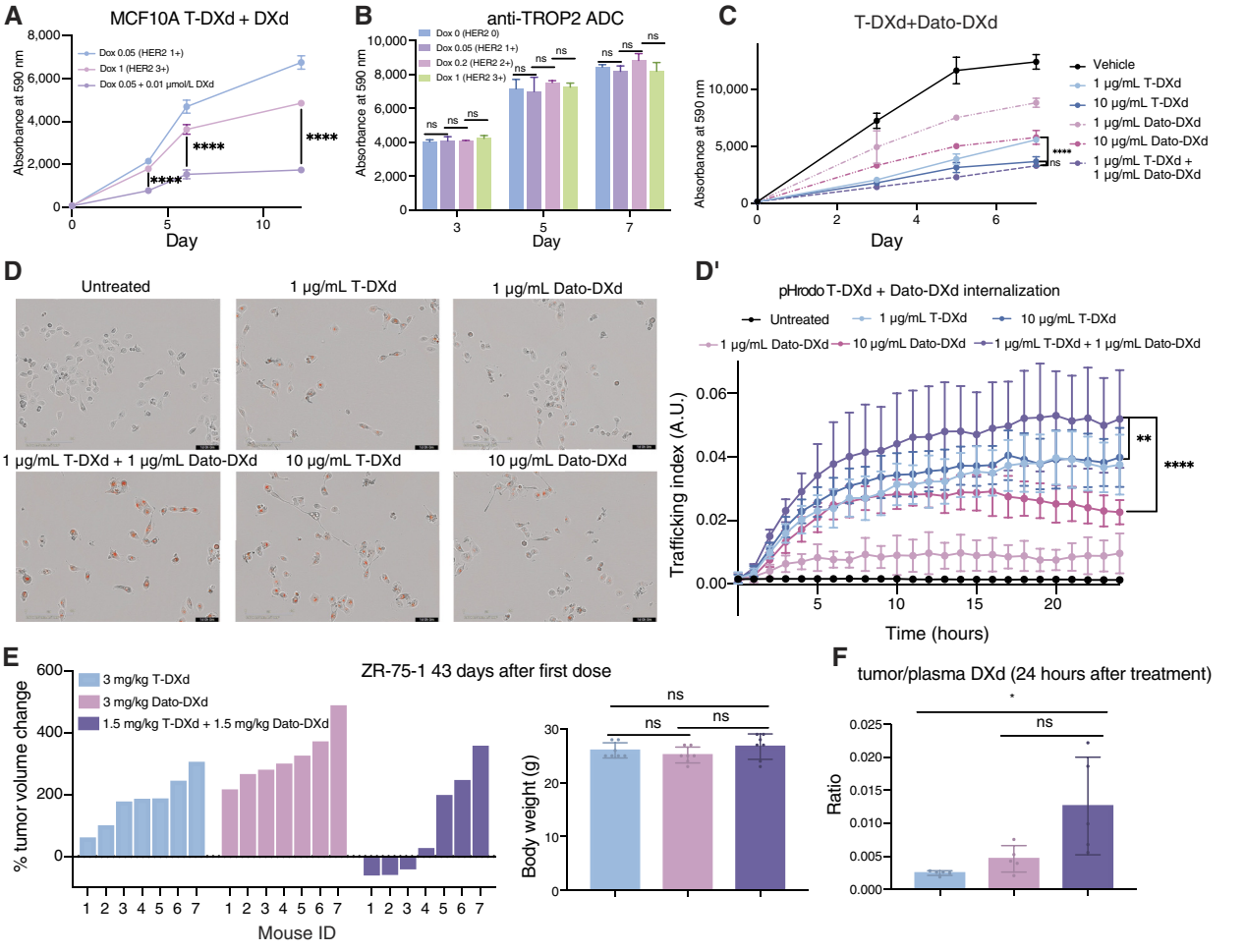


Figure 3. Effects of combined T-DXd and Dato-DXd. **A,** MCF10A treated with 1 μg/mL T-DXd with 0.05 μg/mL (group 1; representing HER2 1+), 1 μg/mL doxycycline induction (group 2; representing HER2 3+), or additional 0.01 μmol/L payload DXd under 0.05 μg/mL doxycycline induction (group 3). Data are presented as the mean ± SD, $n = 3$. *P* values were determined by unpaired two tailed *t* test between groups 2 and 3. ****, $P < 0.0001$. **B,** Number of cells treated with 1 μg/mL anti-TROP2 ADC Dato-DXd under different concentrations of doxycycline (representing different HER2 levels). *P* values were determined by unpaired two tailed *t* test between groups: ns, not significant ($P > 0.05$). **C,** Cell growth curves showing effects of T-DXd, Dato-DXd, and their combination in MCF10A HER2 OE cells induced with 0.2 μg/mL doxycycline. Data are shown as the mean ± SD, $n = 3$. *P* values for the final time point (day 7) between combination of 1 μg/mL T-DXd + 1 μg/mL Dato-DXd with either 10 μg/mL T-DXd or 10 μg/mL Dato-DXd are indicated. ****, $P < 0.0001$; ns, not significant ($P > 0.05$). **D,** Incucyte images showing internalization of pHrodo-labeled T-DXd or Dato-DXd or in combination at 24 hours in MCF10A HER2 OE cells induced with 0.2 μg /mL doxycycline. Statistical analysis is shown in **D′**. Data are presented as the mean ± SD of trafficking index, $n = 12$. Representative plots were shown, with experiments repeated independently three times. Two-way ANOVA analysis with multiple comparisons was performed for each time point. *P* values for the final time point (24 hours) between combination of 1 μg/mL T-DXd + 1 μg/mL Dato-DXd with either 10 μg/mL T-DXd or 10 μg/mL Dato-DXd are indicated. **, $P < 0.01$; ****, $P < 0.0001$. **E,** Left, waterfall plot showing percentage of tumor volume change after 43 days treatment with 3 mg/kg T-DXd, 3 mg/kg Dato-DXd, or combination of 1.5 mg/kg T-DXd+ 1.5 mg/kg Dato-DXd (i.v., once in 3 weeks) in ZR-75-1 CDX. Right, body weight of mice in different treatment groups. Data are shown as the mean ± SD, $n = 7$. *P* values were determined by unpaired two tailed *t* test between groups: ns, not significant ($P > 0.05$). **F,** Ratio of tumor DXd concentrations over plasma DXd concentrations after 24 hours of treatment with 3 mg/kg T-DXd, 3 mg/kg Dato-DXd, or combination of 1.5 mg/kg T-DXd + 1.5 mg/kg Dato-DXd in ZR-75-1 CDX. Data are shown as the mean ± SD, $n = 5$. *P* values were determined by unpaired two tailed *t* test between groups: ns, not significant ($P > 0.05$); *, $P < 0.05$.

expression and ADC response, the role of target expression and ADC–target engagement in therapeutic resistance is not as well characterized (10, 37–39). Herein, we present multiple mechanisms of both intrinsic and acquired *ERBB2* mutations as well as loss of HER2 expression associated with resistance to T-DXd in preclinical models and clinical cohorts.

First, our study revealed a subset of patients who exhibited resistance to T-DXd due to mutations in the extracellular domain of *ERBB2*. Two of these mutations directly disrupted trastuzumab binding whereas a third abrogated HER2 expression, impairing drug internalization and efficacy. Whereas such occurrences are uncommon, the findings illustrate the relevance of target binding to ADC efficacy and also have implications for sequential therapy and the potential for cross-resistance in cases in which ADCs share the same mAb backbone (40). We do note that activating mutations in *ERBB2* (like for patient #3 above) seem to sensitize tumors to HER2-targeted ADCs, because of increased drug internalization and payload delivery, and may lead to prolonged responses even in tumors with very low HER2 expression (22).

Downloaded from aacrjournals.org/cancerdiscovery/article-pdf/16/2/235/3731667/cd-25-0647.pdf by guest on 26 October 2026

Second, we report on loss of HER2 protein expression as a mechanism of resistance to T-DXd. Although true HER2 loss is uncommon in patients with *ERBB2*-amplified breast cancer, this is likely due to HER2 being the key driver of tumor development and progression in this subtype (41, 42). However, in HER2-low cases, in which HER2 is less critical for tumor growth, there is greater potential for HER2 loss. This was reflected from our cohort in which only 1 of 19 cases (5.3%) showed HER2 loss in HER2 3+ patients, 6 of 37 (16.2%) in HER2 2+ patients, and 19 of 46 (41.3%) in HER2 1+ patients. This was also demonstrated in the DAISY trial, in which three patients experienced a drop from IHC 2+ to 1+, 3 from IHC 2+ to 0, and 4 from IHC 1+ to 0, whereas only three patients with IHC 3+ showed a decrease in HER2 expression after T-DXd treatment (10). Similar findings have also been reported after treatment of trastuzumab, T-DM1, as well as next-generation anti-HER2 ADCs, e.g. ARX788 and XMT-1522 (16, 43–46). We note that in a parallel cohort of patients with MBC who received SG, HER2 loss was only observed in 1 of 20 cases (5%), lending support to the hypothesis that HER2 expression changes result from HER2-targeted therapeutic pressure, rather than TOP1 inhibition, or more broad/nonspecific evolutionary changes. We acknowledge the inherent limitations of IHC as a measurement of HER2 expression, as it is influenced by both preanalytic and postanalytic variables that affect interrater reliability—particularly at low expression levels and when using formalin-fixed tissue. It is also unknown whether such HER2 expression changes result from global HER2 downregulation across cancer cells or from selective eradication of HER2-expressing cells (47, 48). Therefore, we utilized IF staining as an independent method and confirmed surface HER2 expression decreased after T-DXd treatment. However, we acknowledge there is limited interpretation resulting from sample availability and technical challenges associated with manual staining and quantification.

Using a series of isogenic cell line models, we demonstrate that such loss of HER2 could directly lead to decreases in T-DXd internalization. The models show that such decrements in T-DXd internalization are tied to significant changes in drug efficacy. This aligns with previous findings showing that enhanced T-DXd trafficking correlates with improved therapeutic response (22). Given these specific changes in drug internalization, we speculated that sensitivity to the payload DXd was ultimately unchanged in these cells. Indeed, addition of low levels of DXd proved effective in the models that had reduced HER2 levels. This prompted investigation into the potential use of an alternative DXd delivery method to overcome resistance.

In models expressing low levels of HER2, addition of a TROP2-targeting ADC, Dato-DXd, proved highly effective. Surprisingly, the data revealed that even low levels of Dato-DXd and T-DXd together could achieve comparable antitumor effects to high doses of the single agents. This finding raises the possibility that saturating dosing of some ADCs may not be necessary for optimal tumor uptake. This suggests that clinical combinations of such agents may not necessarily require the maximally targeted doses to achieve efficacy, providing an avenue to minimize drug toxicity. Overall, the work suggests that combinations of ADCs with distinct antibodies and similar payloads ought to be tested in clinic as a strategy to potentially reduce toxicity and improve efficacy.

This study has several limitations that warrant further investigation. Whereas we have identified resistance mechanisms related to the antigen target, there are other potential biological processes relevant to T-DXd resistance. The roles of the tumor microenvironment, tumor cell plasticity, or DNA damage response/payload resistance were not significantly addressed in this work. With regards to the combinations of ADCs, our studies were limited to conceptual advances regarding internalization but do not address the potential hurdles which may arise in translating these findings to the clinic. Additional studies will be needed, particularly in regard to dose optimization and scheduling, to maximize the therapeutic potential of this approach.

METHODS

Cell Lines

MCF10A, CAMA-1, MCF-7, ZR-75-1, SK-BR-3, and T47D cells were obtained from the ATCC. 293T cells were kindly gifted by Ping Chi's laboratory. Primary cells were derived from tumors of PDXs from the MSKCC antitumor core facility. Cells were tested negative for *Mycoplasma* on a monthly manner using Lonza's MycoAlert Mycoplasma Detection Assays (Lonza #LT07-318). All cells are tested *Mycoplasma*-negative. The latest date when MCF10A cells were tested was May 3, 2025, CAMA-1 was November 11, 2024, MCF-7 was June 19, 2025, ZR-75-1 was June 19, 2025, SK-BR-3 was May 3, 2025, T47D was March 13, 2024, 293T was May 28, 2025, and 18cS1 was November 11, 2024. MCF10A cells (RRID: CVCL_0598) were maintained in DMEM/F12 (Invitrogen #11330-032) supplemented with 5% horse serum (Gibco #16050122), 1% penicillin–streptomycin (Gibco #15140163), 20 ng/mL EGF (PeproTech #AF-100-15), 0.5 mg/mL hydrocortisone (Sigma-Aldrich #H0888), 100 ng/mL cholera toxin (Sigma-Aldrich #C8052), and 10 μg/mL insulin (Sigma-Aldrich #I9278). Primary cells were maintained in mixture of 25% DMEM (Gibco # 12320032) + 75% Ham's F-12 Nutrient Mix (Thermo Fisher Scientific #11765054), supplemented with 5% FBS (Corning #35-010-CV), 5 μg/mL insulin (Sigma-Aldrich #I9278), 0.4 μg/mL hydrocortisone (Sigma-Aldrich #H0888), 20 ng/mL EGF (PeproTech #AF-100–15), 1% penicillin–streptomycin (10,000 U/mL; Gibco #15140163), 1 μmol/L BMP inhibitor DMH-1 (Tocris #4126), 1 μmol/L TGF-β inhibitor A-83-01 (Tocris #2939), 5 μmol/L ROCK inhibitor Y-27623 (Enzo Life Sciences #ALX270-333-M005), and 4 μL/mL adenine (Sigma-Aldrich #A9001). CAMA-1 (RRID: CVCL_1115), 293T, and MCF-7 (RRID: CVCL_0031) cells were maintained in DMEM/F12 medium supplemented with 10% FBS (Corning #35-010-CV) and 1% penicillin–streptomycin (10,000 U/mL; Gibco #15140163). ZR-75-1 (RRID: CVCL_0588), SK-BR-3 (RRID: CVCL_0033), and T47D (RRID: CVCL_0553) cells were cultured in RPMI medium supplemented with 10% FBS (Corning #35-010-CV) and 1% penicillin–streptomycin (10,000 U/mL; Gibco #15140163). Cells were frozen in 90% FBS (Corning #35-010-CV) +10% DMSO (Sigma-Aldrich #D8418), cultured, and used for assays within 10 passages. All cells were maintained in a humidified incubator with 5% CO_2 at 37°C.

Drugs

T-DXd and Dato-DXd were provided by Daiichi Sankyo. Deruxtecan was purchased from MedChemExpress (cat. #HY-13631E).

Downloaded from aacrjournals.org/cancerdiscovery/article-pdf/16/2/235/3731667/cd-25-0647.pdf by guest on 26 October 2026

Drug Reconstitution, Storage, and Dilution

Stock solutions of T-DXd and Dato-DXd were stored at −80°C for long-term preservation. For short-term use, aliquots of 20 μL were prepared and stored at −20°C. Prior to treatment, T-DXd and Dato-DXd were diluted in PBS to the desired concentrations and then added to cell culture medium at a 1:1,000 dilution.

DXd powder was stored at −20°C, protected from light, and freshly prepared before each use. For reconstitution, DXd was dissolved in DMSO at various concentrations and subsequently diluted 1:1,000 into the culture medium.

Patient Specimens

All patients signed written informed consent, and tumor specimens were collected under approved Institutional Review Board (IRB) protocols for NGS (MSKCC IRB #12–245), IHC/IF staining (MSKCC IRB #19-397), and PDX establishment (MSKCC IRB #12–245 and #06–107).

Patient Biopsy HER2 IHC Staining

Assessment of HER2 expression in human samples was conducted in the clinical setting by IHC using formalin-fixed paraffin-embedded (FFPE) sections. The anti-HER2 4B5 clone rabbit mAb (Roche #05999570001, RRID: AB_3101913) was used. HER2 expression was evaluated as per the American Society of Clinical Oncology/College of American Pathologists guidelines in the clinical setting and reviewed by two board-certified pathologists.

Immunoblotting

Cells were incubated with doxycycline (Sigma-Aldrich #9891; ethanol as vehicle) for 48 hours, and the cell pellet was collected. Protein lysates were extracted using RIPA buffer (Thermo Fisher Scientific #89901) supplemented with protease and phosphatase inhibitor (Thermo Fisher Scientific #78446). After 30 minutes of incubation on ice with vortexing every 10 minutes, lysates were centrifuged at 12,000 rpm at 4°C for 30 minutes. The supernatant was obtained and quantified using Pierce BCA Protein Assay (Thermo Fisher Scientific #23223, #23224) by measuring absorbance at 562 nm using SpectraMax iD5. Protein samples were normalized to 2 μg/μL by supplementing with NuPAGE LDS Sample Buffer (4X) (Invitrogen #NP0008) and DL-dithiothreitol (Sigma-Aldrich #D0632-25G) and boiled at 98°C for 5 minute. Electrophoresis was done on SDS-PAGE gels (NuPAGE 4%–12% Bis-Tris Protein Gels, Invitrogen #NP0335BOX) following standard protocol.

Membranes were probed using anti-HER2 rabbit mAb 29D8 (Cell Signaling Technology, cat. #2165, RRID: AB_10692490), anti-β-actin 13E5 (Cell Signaling Technology, cat. #4970, RRID: AB_2223172), anti-TROP2 rabbit mAb D1W5W (Cell Signaling Technology, cat. #90540, RRID: AB_2800160), and anti-vinculin rabbit mAb E1E9V (Cell Signaling Technology, cat. #13901, RRID: AB_2728768). IRDye 800CW anti-rabbit IgG goat secondary antibody (LI-COR Biosciences, cat. #926-32211, RRID: AB_621843) was used. Immobilon Western HRP Substrate (EMD Millipore #WBKLS0500) was used for chemiluminescent detection. BrightCL1000 was used for imaging followed by analysis in Fiji (RRID: SCR_002285; ImageJ2 version 2.14.0/1.54f).

Flow Cytometry

Cells were incubated with doxycycline (Sigma-Aldrich #9891) (ethanol as vehicle) for 48 hours and trypsinized, washed in Cell Staining Buffer (BioLegend #420201), incubated with 5 μL PE anti-human CD340 (erbB2/HER-2) antibody (BioLegend #324406, RRID: AB_756122), and diluted in 100 μL Cell Staining Buffer per sample on ice for 30 minutes in the dark. Cells were washed twice and resuspended in Cell Staining Buffer containing 4′,6-diamidino-2-phenylindole at a final concentration of 0.2 μg/mL (Invitrogen #D3571). Cells were filtered through a 35-μm mesh and analyzed using LSR Fortessa. Data were analyzed using FCS Express 7 Research.

Internalization Assay

T-DXd was labeled with pHrodo using pHrodo Antibody Labeling Kits (Invitrogen #P36014) according to the manufacturer's instructions. Specific amount of cells were seeded to a 96-well Clear Flat Bottom Polystyrene TC-treated Microplate (Corning #3595): MCF10A 1k/well, CAMA-1 3k/well, 18cS1 12k/well, T47D 4k/well, and 293T 2k/well and incubated with specific concentrations of doxycycline overnight. The following day pHrodo T-DXd was added to a final concentration of 5 μg/mL. Incucyte S3 Live-Cell Imaging and Analysis System captured four images per well on both phase and red channels under objective 20× every hour. Integrated intensity of red signal per well was normalized to cells/area/per well and exported as trafficking index (arbitrary unit A.U. is used). Data were analyzed in GraphPad Prism 10.

Cell Viability Assay

Specific amounts of cells were seeded to Falcon 96-well Cell Clear Flat Bottom TC-treated Culture Microplate (Corning #353075): MCF10A 500/well, CAMA-1 1,500/well, 18cS1 3,000/well, T47D 2,000/well, 293T 1,000/well, ZR-75-1 2,000/well, and MCF-7 1,000/well and incubated with doxycycline overnight. The following day, different concentrations of T-DXd or Dato-DXd or combination were added, and cell viability was measured on different days using Resazurin (R&D Systems #AR002), following the standard protocol. Absorbance at 590 nm was measured by SpectraMax M5. Data were analyzed in GraphPad Prism 10.

IHC

For cell line HER2 IHC staining, the cell pellet was embedded in FFPE and sectioned to glass slides. VENTANA DISCOVERY ULTRA instrument was used to perform automatic IHC staining, following the standard protocol. Anti-HER2 rabbit mAb 29D8 (Cell Signaling Technology, cat. #2165, RRID: AB_10692490) was added at 1:200. After staining, slides were washed in soap solution, rinsed with water, immersed in 50%, 70%, 95%, 100%, and 100% ethanol for 5 minutes each, and the immersed in xylene (Sigma-Aldrich #214736) twice for 5 minutes each. Fisher Chemical Permount Mounting Medium (Fisher Scientific #SP15100) was added and covered with Fisherfinest Premium Cover Glasses (Fisher Scientific #12-548-5M).

TROP2 IHC staining was performed at the Molecular Cytology Core Facility of MSKCC using the DISCOVERY ULTRA processor (Ventana Medical Systems). Paraffin-embedded cell pellets were sectioned at 5 μm and baked at 58°C for 1 hour. Slides were prewarmed to 80°C and incubated for 32 minutes, followed by deparaffinization at 72°C. Subsequent steps included pretreatment and cell conditioning.

Slides were then heated to 100°C and incubated for 4 minutes in cell conditioner #1. One drop of Inhibitor Cartridge Module was added and incubated for 8 minutes. The primary antibody, anti-TROP2 Rabbit mAb D1W5W (Cell Signaling Technology, cat. #90540, RRID: AB_2800160), was manually applied at a 1:200 dilution and incubated for 4 hours.

Following primary antibody incubation, one drop of anti-rabbit HRP multimer was applied and incubated for 20 minutes. 3,3′-Diaminobenzidine was used for signal development, and hematoxylin II was applied for counterstaining with an incubation time of 28 minutes. A postcounterstain with reaction buffer was performed, followed by the application of Bluing Reagent, which was incubated for 8 minutes.

Slides were then washed and mounted as per the abovementioned procedure.

Downloaded from aacrjournals.org/cancerdiscovery/article-pdf/16/2/235/3731667/cd-25-0647.pdf by guest on 26 October 2026

Cloning

The *ERBB2* sequence was cloned to pInducer20 plasmid (RRID: Addgene_44012) by gateway cloning following the manufacturer's protocol (Invitrogen # 12535-019).

Site-directed mutagenesis was applied to introduce mutations to pInducer20-HER2:

Primers were designed in https://www.agilent.com/store/primerDesignProgram.jsp.

V597M:

Forward: 5′-GGCAGCGGGCCATGCAGAAGGGAGG-3′
Reverse: 5′-CCTCCCTTCTGCATGGCCCGCTGCC-3′

Q213*:

Forward: 5′-CGTCAGGCTCTAACAATCCTCAGAACTCTCTCC-3′
Reverse: 5′-GGAGAGAGTTCTGAGGATTGTTAGAGCCTGACG-3′

P593R:

Forward: 5′-CCACGCAGAAGGGACGGTCCTTATAGTGG-3′
Reverse: 5′-CCACTATAAGGACCGTCCCTTCTGCGTGG-3′

KAPA HiFi HotStart ReadyMix (Roche #07958927001) was used to perform PCR, followed by restriction digestion of DpnI with CutSmart at 37°C for 3 hours. The product from restriction digestion was transformed to One Shot Stbl3 Chemically Competent *Escherichia coli* (Invitrogen #C737303), following transformation protocol. Single colonies were picked and expanded. Plasmids were extracted using mini-prep (Omega Bio-Tek #D6942-00). Whole plasmid was sequenced through Plasmidsaurus (https://www.plasmidsaurus.com/).

Lentiviral Production

Earlier-passage HEK293T cells were plated in a 10-cm Petri dish at approximately 9 to 10 × 10^6 cells. The medium for cell culture was DMEM (Gibco #11965-092) containing 10% FBS (Gibco #16140-071) and 1X nonessential amino acids (Gibco #11140-050), antibiotic-free preferred. The cells were cultured at 37°C with 5% CO_2 for overnight. The next day, cells were transfected with 5 μg of construct, 4.1 μg of PMD2.G envelop construct (RRID: Addgene_12259), and 7.5 μg of psPAX2 packaging construct (RRID: Addgene_12260) diluted in 0.85 mL Opti-MEM medium (Gibco #31985-062) containing 30 μL X-tremeGENE HP DNA Transfection Reagent (Roche #06366546001). Virus particles from the supernatant were collected after 48 to 72 hours of transfection by filtering the supernatant through a 0.45-μm filter.

DNA Transfection

MCF10A, CAMA-1, 18cS1, T47D, and 293T cells were transduced with lentiviral particles with 8 μg/mL polybrene (Santa Cruz Biotechnology # sc-134220) for 24 hours and cultured in fresh media for another 24 hours. Stably expressing cells were selected by incubating with 500 μg/mL G418 (Invitrogen #ant-gn-5) for 2 weeks.

RT-qPCR

Cells were treated with different doxycycline concentrations for 48 hours. Total RNA was extracted using RNeasy Mini kit (Qiagen #74106) based on the manufacturer's instructions. cDNA was prepared from 1 μg RNA using qScript cDNA Super Mix (VWR #101414-106). RT-qPCR reactions were set up using 50 ng cDNA in 10 μL reactions using TaqMan Fast Advanced Master Mix (Thermo Fisher Scientific #4444964) and the following probes: *ERBB2* (Thermo Fisher Scientific #Hs01007074_g1) and *RPLP0* (housekeeping control; Thermo Fisher Scientific #Hs99999902_m1).

Molecular Dynamics Simulations

We first generated minimum viable structures of both HER2 and trastuzumab to ensure reasonable computational cost of relative alchemical-free energy calculations. This was achieved by adapting an existing crystal structure of HER2 complexed with trastuzumab (PDB ID: 1N8Z). For HER2, an Alphafold2 (RRID: SCR_025454; ref. 49) generated structure of the HER2 extracellular domain IV was used to address the issue that the original 18NZ HER2 structure consisted of an unmodeled linker region between residues 603 to 612. Extracellular domain IV alone was chosen (residues 533–630) as trastuzumab (exclusively) binds this subdomain (23), and this subdomain has been shown to be stably expressed/translated/folded (50). To generate this structure, ColabFold (RRID: SCR_025453; ref. 51) version 1.5.5 was used with default parameters (no relaxation via AMBER, no template information, MMseqs2 for sequence alignment, and three recycles), in which the structure with the highest pLDDT score of the five outputted structures was selected. The Alphafold2 generated structure was aligned using PyMOL (RRID: SCR_000305) to the crystal structure of the subdomain with a backbone RMSD of 0.771 Å. As for trastuzumab, we selected only the variable domains of the antibody joined by an artificial linker domain, as only the variable region mediates the binding with HER2. The light and heavy variable domains are connected by a peptide linker (sequence: SSGGGGSGGGGSGGGGS) into a single-chain variable fragment (scFv), which was originally created for another study (52). Both the Alphafold-generated HER2 subdomain and the trastuzumab scFv were aligned with PyMOL to the 1N8Z structure, generating the starting structure. PDBFixer (https://github.com/openmm/pdbfixer) was used to cap termini, add hydrogens at pH 7.0, and fill in missing residues/atoms.

Alchemical-Free Energy Calculations

We prepared apo and complex unmodified hybrid topology factories for alchemical-free energy calculations (53) using the open-source software package Perses (54), which utilizes its own internal mapping scheme based on a dual topology approach. The structure was solvated in a cube of TIP3P (55) water extending 1.1 nm beyond the structure in each dimension, with 0.15 mol/L NaCl. The systems were parametrized with the Amber 14 ff14SB force field (56). A Monte Carlo Barostat from OpenMM 8.1.1 (57) at 1 atm, 300 k, with a frequency of 50 time steps was set. The positions were minimized using LocalEnergyMinimizer from OpenMM 8.1.1, which searches for the set of particle positions representing a local minima of potential energy using the L-BFGS algorithm (58), with an energy tolerance of 10 kJ/mol and no limit on the maximum number of iterations. Nonequilibrium cycling simulations are then run consisting initially of equilibration at $\lambda = 0$, followed by a forward nonequilibrium process which drives λ from 0 to 1, followed by equilibration at $\lambda = 1$, and ending with the reverse nonequilibrium process driving λ from 1 to 0. Each equilibrium and nonequilibrium step consists of 375,000 steps (at a 4 fs timestep) using a Langevin integrator with BAOAB splitting (59) at a collision rate of 1 picosecond^{-1} and a constraint tolerance of 1e^{-8}, leading to a total trajectory time of 6 nanosecond. 100 replicates were performed per mutation to obtain forward and reverse work distributions. Free energy differences were calculated using the multistate Bennett acceptance ratio (60), which were then used to compute the relative free energy changes across binding, in which $\Delta\Delta G_{binding} = \Delta G_{complex} - \Delta G_{apo}$ Forward and reverse work distributions and trajectories were plotted to assess overlap and convergence, respectively.

ELISA

Cells were seeded in a six-well plate and incubated with different concentrations of doxycycline for 24 hours. The next day, 1 μg/mL T-DXd was added to each well and incubated for 24 hours.

Downloaded from aacrjournals.org/cancerdiscovery/article-pdf/16/2/235/3731667/cd-25-0647.pdf by guest on 26 October 2026

The following day, cells were trypsinized, and cell viability was measured by trypan blue assay. One million viable cells and 1 mL cell medium were collected for each sample with triplicates for each condition. Invitrogen ELISA Buffer Kit (Invitrogen #CNB0011) and NUNC 96-well plate (Fisher #43945) were used for the following ELISA experiment:

Wells were coated with 5 μg/mL coating protein (anti-human IgG, Fc-specific; Sigma-Aldrich #I2136, RRID: AB_260147) using coating buffer A from the kit overnight at 4°C. The next day, plates were washed 3 times with wash buffer with shaking (600 rpm) for 5 minutes each. After washing, 200 μL of assay buffer was added to each well and incubated for 1.5 hours at room temperature (RT) with shaking. The calibration curve was prepared via twofold serial diluting T-DXd in PBS from 500 to 0.5 ng/mL. Cell media samples were prepared by diluting 1:100 in PBS; cell lysate samples were prepared as follows: cell pellet was resuspended in 1,000 μL PBS and homogenized at 6 m/second for 30 seconds. Samples were centrifuged at 12,700 rpm for 15 minutes, and the supernatant was extracted.

A total of 100 μL of each calibrator or sample was plated in duplicate and incubated for 1.5 hours at RT with shaking. After incubation, the plate was washed as previously described. A total of 100 μL of 0.0014 mg/mL anti-human IgG, Fab-specific (Sigma-Aldrich #I2136, RRID: AB_260147) was added to each well and incubated for 1.5 hours at RT with shaking. The plate was washed again as previously described. A total of 100 μL of pNPP substrate (Sigma-Aldrich #P7998) was added to all assay wells. Plates were incubated at RT for 5 to 8 minutes in the dark. A total of 100 μL Stop Solution (1 mol/L NaOH) was added to all wells and read at 405 nm.

IF Microscope

Cells were seeded in Nunc Lab-Tek Chambered Coverglass (Thermo Scientific #155409PK), incubated with 1 μg/mL doxycycline or vehicle control for 24 hours, and Alexa Fluor 488 (Thermo Fisher Scientific #A20181)–labeled T-DXd was added to cells. Six hours later, Molecular Probes LysoTracker Deep Red (Invitrogen #L12492) was added following manual user guide and incubated for 1 hour, followed by incubation with Molecular Probes CellMask Orange Plasma Membrane Stain (Thermo Fisher Scientific #C10045) for 15 minutes. Cells were washed with prewarmed PBS three times and immerse in prewarmed media. A drop of NucBlue Live ReadyProbes Reagent (Hoechst #33342) was added to each chamber. Images were captured with 63X objective using SP5-I. Images were processed and analyzed in Fiji (RRID: SCR_002285; ImageJ2 version 2.14.0/1.54f).

HER2 IF from Patient FFPE Samples

FFPE tissue sections were processed for IF on the Leica Bond automated platform. Following deparaffinization with Leica Bond Dewax, antigen retrieval was performed with Leica Bond Epitope Retrieval solution for 20 minutes. Endogenous peroxidase activity was quenched using the Peroxidase Block from the Leica Microsystems 3P BOND Polymer Refine Detection Kit for 5 minutes. Washes between steps were performed with Leica Microsystems 3P BOND Wash Solution 10X. Slides were then incubated with a rabbit polyclonal anti-HER2 antibody (Enzo Life Sciences #PSC-79-307), followed by polymer reagent application (Leica detection kit), washing, and signal amplification using CF594 Tyramide as the secondary fluorophore.

HER2 IF Imaging and Quantification

Slides were scanned with Pannoramic P250 Flash scanner (3DHistech) using 20x/0.8NA objective lens. Regions of interest around the tissues were then drawn and exported as .tif files from these scans using Slide Viewer (3DHistech). These images were then analyzed using ImageJ/FIJI (NIH). Thresholding was used to measure the total tissue area, positive area, and MFI.

ddPCR to Detect HER2 V597M

An assay specific for the detection of V597M in *ERBB2* was ordered through Bio-Rad (assay ID: dHsaMDS886578889). Cycling conditions were tested to ensure optimal annealing/extension temperature as well as optimal separation of positive from empty droplets. Optimization was done with a known positive control.

After PicoGreen quantification, 9 ng gDNA was combined with locus-specific primers, FAM- and HEX-labeled probes, Hind III, and digital PCR Supermix for probes (no dUTP). All reactions were performed on a QX200 ddPCR system (Bio-Rad #1864001), and each sample was evaluated in technical triplicates. Reactions were partitioned into a median of ~21,000 droplets per well using the QX200 droplet generator. Emulsified PCRs were run on a 96-well thermal cycler using cycling conditions identified during the optimization step (95°C 10′; 40 cycles of 94°C 30′ and 52°C 1′; 98°C 10′; 4°C hold). Plates were read and analyzed with the QuantaSoft software to assess the number of droplets positive for mutant DNA, WT DNA, both, or neither.

In vivo Efficacy Studies

All mouse studies were conducted through the MSKCC antitumor core facility and performed in compliance with institutional guidelines under an Institutional Animal Care and Use Committee–approved protocol (MSKCC #12-10-016).

Tumor tissue from patients with breast cancer was collected under an IRB-approved protocol (MSKCC IRB #12–245 and #06–107). The tissue was immediately minced, mixed (50:50) with Matrigel (Corning), and implanted subcutaneously in 6- to 8-week-old female NOD/SCID gamma (NSG) mice (The Jackson Laboratory) to generate PDXs as previously described (37). Established PDXs (18cS1) were serially transplanted into 6- to 8-week-old NSG mice as above. Once tumors reached an average volume of 100 to 150 mm^3, mice were randomized to receive either a vehicle control (saline), T-DXd alone (3 or 10 mg/kg i.v. once every 3 weeks x2), Dato-DXd alone, (3 mg/kg i.v. once every 3 weeks × 2), or T-DXd (3 mg/kg) + Dato-DXd (3 mg/kg) combinations. Mice were observed daily throughout the treatment period for signs of morbidity/mortality. Tumors were measured twice weekly using calipers, and volume was calculated using the following formula: length × $width^2$ × 0.52. Body weight was also assessed twice weekly. After ~6 weeks of treatment, tumor samples were collected for further analysis.

For the ZR-75-1 CDX model, 5 million cells were implanted subcutaneously in 6- to 8-week-old female NSG mice (The Jackson Laboratory) in the presence of subcutaneous 0.18 mg b-estradiol pellets (Innovative Research of America). Once tumors reached an average volume of 150 mm^3, mice were randomized to receive one of the following treatments: vehicle control (saline), T-DXd alone (3 mg/kg, i.v., once every 3 weeks), Dato-DXd alone (3 mg/kg, i.v., once every 3 weeks), or combination of T-DXd (1.5 mg/kg, i.v.) + Dato-DXd (1.5 mg/kg, i.v.; once every 3 weeks). Tumor measurement and volume calculation were performed as described above.

Pharmacokinetic Study

Six- to 8-week-old female NSG mice (The Jackson Laboratory) were injected subcutaneously with 5 million ZR-75-1 cells in the presence of subcutaneous 0.18 mg b-estradiol pellets (Innovative Research of America). When tumors reached ~ 150 mm^3, mice were randomized into four treatment groups (n = 5/group) and administered either a control vehicle or T-DXd (3 mg/kg), Dato-DXd (3 mg/kg), or their combination (1.5 mg/kg each) via intravenous injection once. Plasma and tumors were collected 24 hours later. Plasma samples (100 μL) were protein-precipitated with 500 μL cold acetonitrile before centrifugation at 4°C for 10 minutes at 12,700 rpm. The supernatant was

Downloaded from aacrjournals.org/cancerdiscovery/article-pdf/16/2/235/3731667/cd-25-0647.pdf by guest on 26 October 2026

dried and resuspended in 200 μL acetonitrile for LC-MS analysis. For tumor tissue preparation, each sample was placed into a homogenization tube with ceramic beads with 500 μL acetonitrile. Tubes were run for 30 seconds at 6 m/second on a BeadMill24 (Thermo Fisher Scientific) before centrifugation at 12,700 rpm for 10 minutes at 4°C. The supernatant was placed in new tubes and dried as above. Following complete drying, samples were resuspended in 200 μL of acetonitrile for LC-MS analysis. Both sets of samples were run on an Agilent 6475A Triple Quadrupole LC-MS/MS. MS parameters: m/z = 494.2 > 375.1. Solvent conditions were 0.1% formic acid in HPLC-grade water for the aqueous phase and 0.1% formic acid in acetonitrile for the organic phase. Drug-spiked plasma calibrations were performed, with linear values ranging from 10 ng/mL to 10 μg/mL.

Statistical Analyses

Statistical analyses were performed in GraphPad Prism (RRID: SCR_002798) version 10.2.3 (347). Two-way ANOVA test with multiple comparisons was performed for internalization assay. Unpaired two tailed test was performed for ELISA quantification and cell viability assay. *In vivo* data are presented as the mean ± SEM, all other data are represented as the mean ± SD, and the exact *P* values are indicated under each condition.

Data Availability

All input files and relevant structures for computational modeling and ΔΔG estimation of V597M are available online on GitHub (https://github.com/joshualausj/HER2_V597M). From these files, the relevant hybrid topology factories (HTF) and work trajectories (NPY) can be regenerated by following the instructions. The previously generated HTF, NPY, and analysis files are available on OSF (https://osf.io/zd8xr/). All methods described above are open-source, and their source code is available online on GitHub for Perses (https://github.com/choderalab/perses), OpenMM (https://openmm.org/), and OpenMMTools (https://github.com/choderalab/openmmtools).

Authors' Disclosures

W. Chen reports grants from Daiichi Sankyo during the conduct of the study. N. Mai reports grants from Merck outside the submitted work. J.D. Chodera reports grants from the National Institutes of Health, personal fees and other support from Achira, personal fees from OpenEye Scientific Software, and nonfinancial support from BIH Einstein Foundation Visiting Professorship outside the submitted work. The Chodera laboratory receives or has received funding from multiple sources, including the National Institutes of Health, the National Science Foundation, the Parker Institute for Cancer Immunotherapy, Relay Therapeutics, Entasis Therapeutics, Silicon Therapeutics, EMD Serono (Merck KGaA), AstraZeneca, Vir Biotechnology, Bayer, XtalPi, Interline Therapeutics, the Molecular Sciences Software Institute, the Starr Cancer Consortium, the Open Force Field Consortium, Cycle for Survival, a Louis V. Gerstner Young Investigator Award, and the Memorial Sloan Kettering Institute. A complete funding history for the Chodera laboratory can be found at http://choderalab.org/funding. F. Pareja reports personal fees from AstraZeneca and MultiplexDx outside the submitted work. S. Modi reports grants and personal fees from AstraZeneca, Daiichi Sankyo, Genentech, Pfizer, and Seagen, grants from D3Bio and Biontech, and personal fees from Gilead during the conduct of the study, as well as grants and personal fees from AstraZeneca, Daiichi Sankyo, Genentech, Pfizer, and Seagen, grants from BioNTech and D3Bio, and personal fees from Gilead outside the submitted work. P. Razavi reports grants and personal fees from Myriad, Foresight, SAGA Diagnostics, SOPHIA Genetics, Natera, Novartis, AstraZeneca, and NeoGenomics, grants from Guardant, Personalis, Biodesix, Roche, Grail, and Biothernostics, grants and nonfinancial support from Tempus, personal fees and nonfinancial support from Lilly/Loxo, and personal fees from Biovica, Prelude Therapeutics, Stemline Therapeutics, Regor Pharmaceuticals, and pathos.ai during the conduct of the study. J.Z. Drago reports grants and personal fees from AstraZeneca, personal fees from Genagon, AmMax Bio, NuProbe, Revelio Therapeutics, MEDACorp, and Baird Conferences, and grants from Merck outside the submitted work. S. Chandarlapaty reports grants from Daiichi Sankyo during the conduct of the study, as well as grants and personal fees from AstraZeneca and personal fees from Daiichi Sankyo, Merck, Casdin Capital, Novartis, Nuvalent, Lilly, and pathos.ai outside the submitted work. No disclosures were reported by the other authors.

Authors' Contributions

W. Chen: Conceptualization, resources, data curation, software, formal analysis, validation, investigation, visualization, methodology, writing–original draft, project administration, writing–review and editing. **A. Gupta:** Conceptualization, data curation, validation, investigation, methodology, writing–original draft, writing–review and editing. **N. Mai:** Conceptualization, data curation, formal analysis, investigation, writing–original draft, writing–review and editing. **S. Nag:** Data curation, writing–review and editing. **J.S. Lau:** Data curation, software, formal analysis, methodology, writing–original draft. **S. Singh:** Data curation, software, formal analysis, methodology, writing–original draft. **J.D. Chodera:** Resources, investigation. **B. Liu:** Conceptualization, validation, methodology. **E. de Stanchina:** Resources, supervision, investigation. **F. Pareja:** Data curation. **A.A. Hashmi:** Data curation. **M.M. Lieberman:** Data curation. **S. Modi:** Data curation. **J. Bromberg:** Data curation. **P. Razavi:** Project administration. **J.Z. Drago:** Conceptualization, formal analysis, supervision, investigation, writing–original draft. **S. Chandarlapaty:** Conceptualization, resources, data curation, supervision, funding acquisition, investigation, writing–original draft, writing–review and editing.

Acknowledgments

The Chandarlapaty laboratory has received generous funding support for this research from the NIH (1R01CA249666-01A) and the Breast Cancer Research Foundation (BCRF-24-185). We acknowledge the use of the Flow Cytometry, Antitumor Assessment, Pathology, Gene Editing & Screening, Integrated Genomics Operation and Molecular Cytology Core Facility at MSKCC, funded in part through the NIH/NCI Cancer Center Support Grant P30 CA008748. J.Z. Drago received funding from the Sussman Family Fund. E. de Stanchina received funding form P30 CA008748 S5. F. Pareja is supported in part by an NIH P50 CA247749-01 grant and an FDA 1U01FD007909-01A1 grant. We thank Dr. Dara S. Ross for performing FISH and processing images of HER2-mutant samples; Jianmin Yang for help in lentiviral production; Cassidy Cobbs and Andrea Farina for help designing and performing ddPCR; Sydney Bowker, Inna Khodos, and Akiba Waterman for help in *in vivo* efficacy studies; Santosh Adiraju, Gabriel Weidler, and Vanessa Thompson for help in PK studies; Eric Chan and Shevin Narine for help in HER2 patient sample IF; and Shevin Narine and Ning Fan for help in preparing FFPE sections of cell pellets and TROP2 IHC staining.

Note

Supplementary data for this article are available at Cancer Discovery Online (http://cancerdiscovery.aacrjournals.org/).

Received April 15, 2025; revised September 26, 2025; accepted November 5, 2025; Posted first November 10, 2025.

Downloaded from aacrjournals.org/cancerdiscovery/article-pdf/16/2/235/3731667/cd-25-0647.pdf by guest on 26 October 2026

REFERENCES

1. Colombo R, Tarantino P, Rich JR, LoRusso PM, de Vries EGE. The journey of antibody–drug conjugates: lessons learned from 40 years of development. Cancer Discov 2024;14:2089–108.
2. Tsao L-C, Wang JS, Ma X, Sodhi S, Ragusa JV, Liu B, et al. Effective extracellular payload release and immunomodulatory interactions govern the therapeutic effect of trastuzumab deruxtecan (T-DXd). Nat Commun 2025;16:3167.
3. Loibl S, Gianni L. HER2-positive breast cancer. Lancet 2017;389: 2415–29.
4. Verma S, Miles D, Gianni L, Krop IE, Welslau M, Baselga J, et al. Trastuzumab emtansine for HER2-positive advanced breast cancer. N Engl J Med 2012;367:1783–91.
5. von Minckwitz G, Huang C-S, Mano MS, Loibl S, Mamounas EP, Untch M, et al. Trastuzumab emtansine for residual invasive HER2-positive breast cancer. N Engl J Med 2019;380:617–28.
6. Cortés J, Kim S-B, Chung W-P, Im S-A, Park Y-H, Hegg R, et al. Trastuzumab deruxtecan versus trastuzumab emtansine for breast cancer. N Engl J Med 2022;386:1143–54.
7. Ogitani Y, Aida T, Hagihara K, Yamaguchi J, Ishii C, Harada N, et al. DS-8201a, a novel HER2-targeting ADC with a novel DNA topoisomerase I inhibitor, demonstrates a promising antitumor efficacy with differentiation from T-DM1. Clin Cancer Res 2016;22:5097–108.
8. Nakada T, Sugihara K, Jikoh T, Abe Y, Agatsuma T. The latest research and development into the antibody–drug conjugate, [fam-] trastuzumab deruxtecan (DS-8201a), for HER2 cancer therapy. Chem Pharm Bull (Tokyo) 2019;67:173–85.
9. Modi S, Jacot W, Yamashita T, Sohn J, Vidal M, Tokunaga E, et al. Trastuzumab deruxtecan in previously treated HER2-low advanced breast cancer. N Engl J Med 2022;387:9–20.
10. Mosele F, Deluche E, Lusque A, Le Bescond L, Filleron T, Pradat Y, et al. Trastuzumab deruxtecan in metastatic breast cancer with variable HER2 expression: the phase 2 DAISY trial. Nat Med 2023;29:2110–20.
11. Bardia A, Hu X, Dent R, Yonemori K, Barrios CH, O'Shaughnessy JA, et al. Trastuzumab deruxtecan after endocrine therapy in metastatic breast cancer. N Engl J Med 2024;391:2110–22.
12. Drago JZ, Modi S, Chandarlapaty S. Unlocking the potential of antibody–drug conjugates for cancer therapy. Nat Rev Clin Oncol 2021;18:327–44.
13. Abelman RO, Wu B, Spring LM, Ellisen LW, Bardia A. Mechanisms of resistance to antibody–drug conjugates. Cancers (Basel) 2023;15:1278.
14. Bon G, Pizzuti L, Laquintana V, Loria R, Porru M, Marchiò C, et al. Loss of HER2 and decreased T-DM1 efficacy in HER2 positive advanced breast cancer treated with dual HER2 blockade: the SePHER Study. J Exp Clin Cancer Res 2020;39:279.
15. Tarantino P, Ajari O, Graham N, Vincuilla J, Parker T, Hughes ME, et al. Evolution of HER2 expression between pre-treatment biopsy and residual disease after neoadjuvant therapy for breast cancer. Eur J Cancer 2024;201:113920.
16. Loganzo F, Tan X, Sung M, Jin G, Myers JS, Melamud E, et al. Tumor cells chronically treated with a trastuzumab–maytansinoid antibody–drug conjugate develop varied resistance mechanisms but respond to alternate treatments. Mol Cancer Ther 2015;14:952–63.
17. Li G, Guo J, Shen B-Q, Yadav DB, Sliwkowski MX, Crocker LM, et al. Mechanisms of acquired resistance to trastuzumab emtansine in breast cancer cells. Mol Cancer Ther 2018;17:1441–53.
18. Coates JT, Sun S, Leshchiner I, Thimmiah N, Martin EE, McLoughlin D, et al. Parallel genomic alterations of antigen and payload targets mediate polyclonal acquired clinical resistance to sacituzumab govitecan in triple-negative breast cancer. Cancer Discov 2021;11:2436–45.
19. Gouda MA, Gonugunta A, Dumbrava EE, Yap TA, Rodon J, Piha-Paul SA, et al. Human epidermal growth factor receptor 2 loss following treatment with trastuzumab deruxtecan in patients with metastatic breast cancer. Clin Cancer Res 2025;31:1268–74.
20. Martin LP, Konner JA, Moore KN, Seward SM, Matulonis UA, Perez RP, et al. Characterization of folate receptor alpha (FRα) expression in archival tumor and biopsy samples from relapsed epithelial ovarian cancer patients: A phase I expansion study of the FRα-targeting antibody-drug conjugate mirvetuximab soravtansine. Gynecol Oncol 2017;147:402–7.
21. Goto K, Goto Y, Kubo T, Ninomiya K, Kim S-W, Planchard D, et al. Trastuzumab deruxtecan in patients with HER2-mutant metastatic non–small-cell lung cancer: primary results from the randomized, phase II DESTINY-lung02 trial. J Clin Oncol 2023;41:4852–63.
22. Li BT, Michelini F, Misale S, Cocco E, Baldino L, Cai Y, et al. HER2-Mediated internalization of cytotoxic agents in ERBB2 amplified or mutant lung cancers. Cancer Discov 2020;10:674–87.
23. Cho H-S, Mason K, Ramyar KX, Stanley AM, Gabelli SB, Denney DW, et al. Structure of the extracellular region of HER2 alone and in complex with the Herceptin Fab. Nature 2003;421:756–60.
24. Cheng DT, Mitchell TN, Zehir A, Shah RH, Benayed R, Syed A, et al. Memorial sloan kettering-integrated mutation profiling of actionable cancer targets (MSK-IMPACT): a hybridization capture-based next-generation sequencing clinical assay for solid tumor molecular oncology. J Mol Diagn 2015;17:251–64.
25. Chakravarty D, Gao J, Phillips S, Kundra R, Zhang H, Wang J, et al. OncoKB: a precision oncology knowledge base. JCO Precis Oncol 2017. [Epub ahead of print].
26. Petljak M, Maciejowski J. Molecular origins of APOBEC-associated mutations in cancer. DNA Repair (Amst) 2020;94:102905.
27. Gupta A, Gazzo A, Selenica P, Safonov A, Pareja F, da Silva EM, et al. APOBEC3 mutagenesis drives therapy resistance in breast cancer. Nat Genet 2025;57:1452–62.
28. Drago JZ, Pareja F, Jhaveri KL, Walsh EM, Ku GY, Maron SB, et al. HER2 persistence after treatment with T-DXd in breast and gastrointestinal cancers. J Clin Oncol 2023;41(Suppl 16):1052.
29. Engel KB, Moore HM. Effects of preanalytical variables on the detection of proteins by immunohistochemistry in formalin-fixed, paraffin-embedded tissue. Arch Pathol Lab Med 2011;135:537–43.
30. Bagchi A, Madaj Z, Engel KB, Guan P, Rohrer DC, Valley DR, et al. Impact of preanalytical factors on the measurement of tumor tissue biomarkers using immunohistochemistry. J Histochem Cytochem 2021;69:297–320.
31. Bardia A, Krop IE, Kogawa T, Juric D, Tolcher AW, Hamilton EP, et al. Datopotamab deruxtecan in advanced or metastatic HR+/HER2– and triple-negative breast cancer: results from the phase I TROPION-PanTumor01 study. J Clin Oncol 2024;42:2281–94.
32. Bardia A, Jhaveri K, Kalinsky K, Pernas S, Tsurutani J, Xu B, et al. TROPION-Breast01: datopotamab deruxtecan vs chemotherapy in pre-treated inoperable or metastatic HR+/HER2– breast cancer. Future Oncol 2024;20:423–36.
33. Dent RA, Cescon DW, Bachelot T, Jung KH, Shao Z-M, Saji S, et al. TROPION-Breast02: datopotamab deruxtecan for locally recurrent inoperable or metastatic triple-negative breast cancer. Future Oncol 2023;19:2349–59.
34. Singh AP, Sharma S, Shah DK. Quantitative characterization of in vitro bystander effect of antibody-drug conjugates. J Pharmacokinet Pharmacodyn 2016;43:567–82.
35. Mak SY, Chen S, Fong WJ, Choo A, Ho YS. A simple and highly sensitive LC–MS workflow for characterization and quantification of ADC cleavable payloads. Sci Rep 2024;14:11018.
36. Koganemaru S, Kawai T, Fuchigami H, Maeda N, Koyama K, Kuboki Y, et al. Quantitative analysis of drug distribution in heterogeneous tissues using dual-stacking capillary electrophoresis–mass spectrometry. Br J Pharmacol 2023;180:762–74.
37. Meric-Bernstam F, Makker V, Oaknin A, Oh D-Y, Banerjee S, González-Martín A, et al. Efficacy and safety of trastuzumab deruxtecan in patients with HER2-expressing solid tumors: primary results from the DESTINY-PanTumor02 phase II trial. J Clin Oncol 2024;42:47–58.
38. Eisses B, van Geel JJL, Brouwers AH, Bensch F, Elias SG, Kuip EJM, et al. Whole-body HER2 heterogeneity identified on HER2 PET in HER2-negative, -low, and -positive metastatic breast cancer. J Nucl Med 2024;65:1540–7.
39. Gao Y, Yin L, Duan X, Fu Z, Liu Q, Chen J, et al. HER2-targeted PET/CT imaging provides potential biomarkers for differentiating HER2-zero, -low, and -positive breast cancer. Eur J Nucl Med Mol Imaging 2025;52:4525–38.

Downloaded from aacrjournals.org/cancerdiscovery/article-pdf/16/2/235/3731667/cd-25-0647.pdf by guest on 26 October 2026

40. Khoury T, Mojica W, Hicks D, Starostik P, Ademuyiwa F, Janarthanan B, et al. ERBB2 juxtamembrane domain (trastuzumab binding site) gene mutation is a rare event in invasive breast cancers overexpressing the ERBB2 gene. Mod Pathol 2011;24:1055–9.
41. Moasser MM. The oncogene HER2: its signaling and transforming functions and its role in human cancer pathogenesis. Oncogene 2007; 26:6469–87.
42. Gutierrez C, Schiff R. HER2: biology, detection, and clinical implications. Arch Pathol Lab Med 2011;135:55–62.
43. Xiao C, Gong Y, Han EY, Gonzalez-Angulo AM, Sneige N. Stability of HER2-positive status in breast carcinoma: a comparison between primary and paired metastatic tumors with regard to the possible impact of intervening trastuzumab treatment. Ann Oncol 2011;22:1547–53.
44. Barok M, Le Joncour V, Martins A, Isola J, Salmikangas M, Laakkonen P, et al. ARX788, a novel anti-HER2 antibody-drug conjugate, shows anti-tumor effects in preclinical models of trastuzumab emtansine-resistant HER2-positive breast cancer and gastric cancer. Cancer Lett 2020;473:156–63.
45. Le Joncour V, Martins A, Puhka M, Isola J, Salmikangas M, Laakkonen P, et al. A novel anti-HER2 antibody–drug conjugate XMT-1522 for HER2-positive breast and gastric cancers resistant to trastuzumab emtansine. Mol Cancer Ther 2019;18:1721–30.
46. Pectasides D, Gaglia A, Arapantoni-Dadioti P, Bobota A, Valavanis C, Kostopoulou V, et al. HER-2/neu status of primary breast cancer and corresponding metastatic sites in patients with advanced breast cancer treated with trastuzumab-based therapy. Anticancer Res 2006;26:647–53.
47. Press MF, Cordon-Cardo C, Slamon DJ. Expression of the HER-2/neu proto-oncogene in normal human adult and fetal tissues. Oncogene 1990;5:953–62.
48. Robbins CJ, Fernandez AI, Han G, Wong S, Harigopal M, Podoll M, et al. Multi-institutional assessment of pathologist scoring HER2 immunohistochemistry. Mod Pathol 2023;36:100032.
49. Jumper J, Evans R, Pritzel A, Green T, Figurnov M, Ronneberger O, et al. Highly accurate protein structure prediction with AlphaFold. Nature 2021;596:583–9.
50. Jost C, Schilling J, Tamaskovic R, Schwill M, Honegger A, Plückthun A. Structural basis for eliciting a cytotoxic effect in HER2-overexpressing cancer cells via binding to the extracellular domain of HER2. Structure 2013;21:1979–91.
51. Mirdita M, Schütze K, Moriwaki Y, Heo L, Ovchinnikov S, Steinegger M. ColabFold: making protein folding accessible to all. Nat Methods 2022;19:679–82.
52. Okazaki K, Kobashigawa Y, Morita H, Yamauchi S, Fukuda N, Liu C, et al. Molecular dynamics-based design and biophysical evaluation of thermostable single-chain fv antibody mutants derived from pharmaceutical antibodies. ACS Omega 2023;8:22945–54.
53. Mey ASJS, Allen BK, Macdonald HEB, Chodera JD, Hahn DF, Kuhn M, et al. Best practices for alchemical free energy calculations [Article v1.0]. Living J Comput Mol Sci 2020;2, 18378.
54. Zhang I, Rufa DA, Pulido I, Henry MM, Rosen LE, Hauser K, et al. Identifying and overcoming the sampling challenges in relative binding free energy calculations of a model protein:protein complex. J Chem Theor Comput 2023;19:4863–82.
55. MacKerell AD, Bashford D, Bellott M, Dunbrack RL, Evanseck JD, Field MJ, et al. All-atom empirical potential for molecular modeling and dynamics studies of proteins. The J Phys Chem B 1998;102: 3586–616.
56. Maier JA, Martinez C, Kasavajhala K, Wickstrom L, Hauser KE, Simmerling C. ff14SB: improving the accuracy of protein side chain and backbone parameters from ff99SB. J Chem Theor Comput 2015;11:3696–713.
57. Eastman P, Galvelis R, Peláez RP, Abreu CRA, Farr SE, Gallicchio E, et al. OpenMM 8: molecular dynamics simulation with machine learning potentials. J Phys Chem B 2024;128:109–16.
58. Liu DC, Nocedal J. On the limited memory BFGS method for large scale optimization. Math Program 1989;45:503–28.
59. Bussi G, Parrinello M. Accurate sampling using Langevin dynamics. Phys Rev E Stat Nonlin Soft Matter Phys 2007;75:056707.
60. Shirts MR, Chodera JD. Statistically optimal analysis of samples from multiple equilibrium states. J Chem Phys 2008;129:124105.

Downloaded from aacrjournals.org/cancerdiscovery/article-pdf/16/2/235/3731667/cd-25-0647.pdf by guest on 26 October 2026